CONF-8505189--5

PAIR PRODUCTION AT GeV/u ENERGIES

C. Bottcher and M. R. Strayer
Physics Division
Oak Ridge National Laboratory
Oak Ridge, Tennessee 37831

MASTER

CONF-8505189--5

DE86 008986

invited paper

to be published in

Proceedings of the Atomic Theory Workshop on Relativistic and QED Effects in Heavy Atoms

National Bureau of Standards
Gaithersburg, Maryland 20899
May 23-24, 1985

DISCLAIMER

PAIR PRODUCTION AT GeV/u ENERGIES*

C. Bottcher and M. R. Strayer
Physics Division, Oak Ridge National Laboratory
Oak Ridge, Tennessee 37831

ABSTRACT

Electron and positron production in relativistic ion-atom collisions is discussed within the context of the time-dependent Dirac-Hartree approximation to a fully relativistic field theory of the collision. The time-dependent fields are treated classically, and the numerical methods employing basis splines are discussed in detail and contrasted with results obtained from the case of non-relativistic velocities. The results of a one-dimensional model are presented and show a moderately large probability for pair production followed by electron capture.

INTRODUCTION

We propose to discuss electron and positron production in collisions between heavy ions moving at relative velocities exceeding half the speed of light. Using the notation A,B for bare nuclei [e.g. U,Cm] and A(n) for a nucleus associated with a single electron in state n, delta-electron production may be written,

$$A + B(1s) \rightarrow A + B + e^-(E > mc^2). \qquad (1)$$

Positron production may be pictured as the removal of an electron from the Dirac sea,

$$A + B + e^-(E < -mc^2) \rightarrow A + B(1s). \qquad (2)$$

If we time reverse (2), we see that both processes are in essence no different from the ionization phenomena familiar in low energy atomic physics. Unless otherwise stated, m is the electron mass.

While the systems experimentally studied so far should strictly be treated as many electron problems, we believe that the independent particle model is a good first approximation to the relativistic phenomena considered, and we shall use this language throughout in the interest of clarity.

Heretofore theoretical and experimental studies of pair production[1,2] have focused on relative collision velocities around 0.1c. At these velocities two heavy nuclei just touch at the classical turning point of the collision, thus maximizing the time during which

*Research sponsored in part by the U.S. Department of Energy under contract DE-AC05-84OR21400 with Martin Marietta Energy Systems, Inc.

a combined "supercritical" system can be said to exist. The possibility of forming a long-lived nuclear molecule is also maximized, since at higher velocities binary and ternary fission results in a rapid decay of the supercritical system.

The present work has two motivations We are interested in relativistic many-body problems in nuclear and particle physics, e.g. dynamics of hadronic matter and the confinement of quarks in hadrons. It would seem appropriate to begin by understanding the relativistic many-electron problem for which we believe we can write down a correct formalism. From other articles in this volume, it is clear that the relativistic many-electron system is very much an open problem, even as regards bound-state calculations. In either atomic or nuclear physics, the dynamical problem is almost untouched. A more practical motivation is to calculate possible charge changing mechanisms which might affect the design of a relativistic heavy ion collider, as discussed in this volume by H. Gould. Other applications may be found in the realm of heavy-ion-induced fusion, in which interest has recently been revived.

Based on preliminary calculations (described below), we reach the conclusion that atomic phenomena do not "run out" at GeV energies, but become more rich and interesting, and continue so to energies as high as we are likely to reach experimentally in the near future.

The processes (1) and (2) can be better understood from Fig. 1 which illustrates the spectrum of an electron in the field of a heavy nucleus. Our approach is conceptually very simple: we integrate the single-particle, time-dependent Dirac equation

$$H_D \psi = i \frac{\partial \psi}{\partial t} \tag{3}$$

where H_D contains the external vector potential of the moving nuclei. Initially ψ corresponds to a 1s state; at the end of the collision, we project onto the discretized spectrum of the final state Hamiltonian to obtain the probabilities for (1) or (2),

$$p_n = \left| \langle \phi_n | \psi \rangle \right|^2 \tag{4}$$

This process is explained in detail in Section 5 below. We must stress that the time integration is achieved by representing ψ as a superposition of space localized finite elements: until the last step (4), we do not deal with a basis of eigenfunctions. It is also worth repeating that the positron production (2) is computed by time reversing the physical process.

We conclude this section by noting that we shall use a system of units natural to the Dirac equation:

energy	mc^2	511 keV
length	αa_o	386 fm
time	$\alpha^2 t_o$	1.21×10^{-21} s

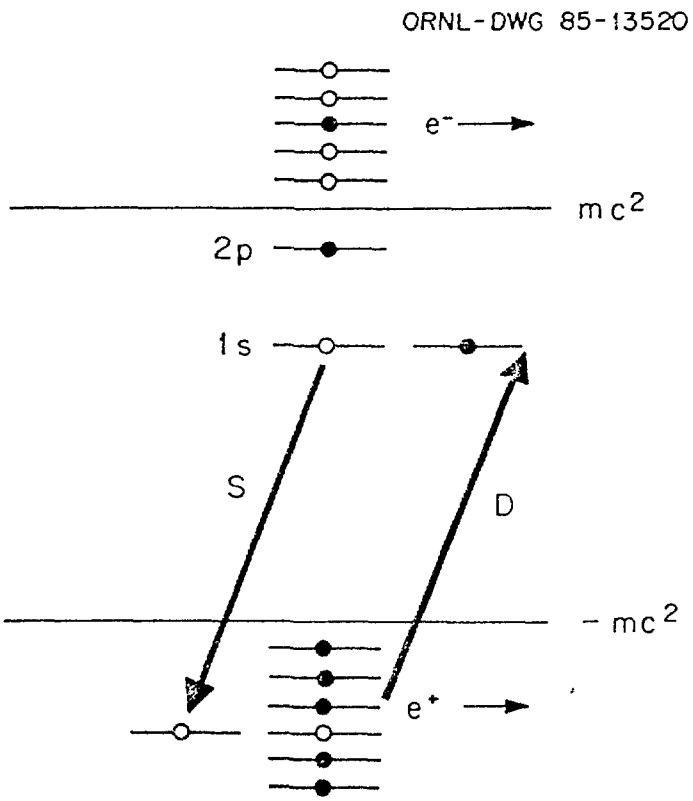

Fig. 1. Energy spectrum of particle and hole states for an electron in the field of a heavy nucleus. The arrows S and D distinguish schematically the spontaneous and dynamical mechanisms of positron production (Ref. 1).

Then the equations can be written with m=c=h=1; however, we sometimes display m in the interests of clarity. The above length is the Compton wavelength of the electron, and the time unit is also natural for nuclear heavy-ion processes. This reflects in part the relativistic collapse of the electronic orbit to nuclear dimensions in the presence of very strong fields. Figure 2 shows the three length scales which enter pair production problems for a U atom: the radius of the U nucleus, the Compton wavelength of the electron, and the radius of the U K-shell. When an electron approaches within αa_0 of a heavy nucleus, its potential energy becomes comparable with mc^2. As two heavy nuclei are brought together slowly, the K-shell radius collapses from a few αa_0 to ~$0.2\ \alpha a_0$, nearly the size of the nucleus.

PAIR PRODUCTION RESULTS AT A FEW MeV/u

We shall not labor the results of our earlier calculations at collision velocities ~0.1c since they are adequately described in

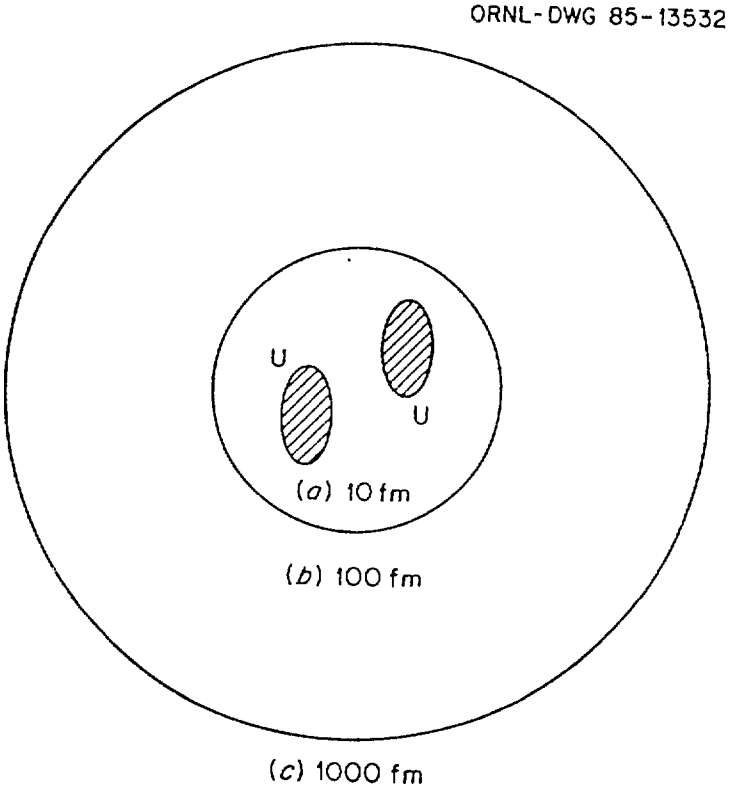

Fig. 2. Length scales in a collision between two heavy ions: (a) nuclear radius; (b) electron Compton wavelength; (c) radius of uranium K-shell.

Ref. 2 and in a more extensive forthcoming article. However, we feel it is worthwhile to highlight the undoubted insights derived from our numerical approach.

Our Hamiltonian is based on the monopole approximation which is well established for relative velocities up to ~0.3c. Since electron and positron production are dominated by the rapid collapse of the K-shell when the nuclei approach within $0.3\ \alpha a_0$, it is a good approximation to expand the projectile and target interactions about some point on the internuclear axis and retain only the monopole terms. At higher velocities the retarded electrostatic and magnetic interactions break the monopole symmetry and indeed all the symmetries of three-space dimensions. We have been able to confirm many of the earlier predictions of the Frankfurt group at the 20% level of accuracy, a significant achievement in view of the vast differences in the two approaches.

The numerical method has enabled us to unify the apparently physically distinct mechanisms of spontaneous and dynamical positron production. In the spontaneous mechanism we imagine the 1s hole energy adiabatically depressed to an energy $E < -mc^2$: an electron in

the Dirac sea then spontaneously decays into the depressed state creating a positron of energy $|E|$ (see Fig. 1). This decay has a natural width of about one KeV. In the dynamical mechanism the time Fourier components of the perturbation induce transitions from the Dirac sea to the 1s hole. However, if we imagine that the collision time is tuned from a small value to values which are comparable to or larger than the spontaneous decay time of about 10^{-20} sec, then the dynamical process must slide continuously into the spontaneous. In the adiabatic basis method[1] the 1s hole must be represented as a decaying state whose rate of decay is separately calculated. By contrast both limits emerge natually from the numerical solution of the time-dependent Dirac equation. We can demonstrate how this works by considering a head-on U + Cm collision at 6.05 MeV/u.

In Fig. 3c is plotted the perturbation in the wavefunction (initially a Cm 1s state) at the distance of closest approach as a function of the distance from the Cm nucleus. Figure 3d shows the result of introducing a time delay by simply holding the nuclei fixed for a period $T = 50\ \alpha^2 t_o$: the localized state has decayed into an outgoing Coulomb wave at large distances. In Fig. 3a,b are plotted the amounts of probability in the continua $E > mc^2$, $< -mc^2$ as a function of time: these are calculated by projecting on eigenstates of the final-state Hamiltonian. We see that while the nuclei are fixed, electron probability is converted into positron probability which is observed as a sharp spike in the positron emission spectrum. Figure 4 shows the positron spectrum as a function of our "ad hoc" time delay T. The broad hump at $T = 0$ evolves continuously into an oscillatory structure and ultimately a single sharp peak. The merits and shortcomings of the long-lived nuclear state hypothesis are discussed elsewhere in these proceedings. We merely note here that the peak position is sensitive to the impact parameter and target charge (Fig. 4d).

Figures 3 and 4 make a further point which probably applies to all energetic ion-atom collisions. The wavefunctions are highly localized in space and present a rather simple picture which is easy to interpret. As a corollary, the Fourier components of the wavefunction are spread over a wide range of momenta and present a complicated picture. For these reasons, we believe that numerical methods which represent the wavefunction in space offer the best hope for future progress.

RELATIVISTIC ION-ATOM COLLISIONS

Consider a system of electrons moving under the influence of an external current provided by the motion of one or more heavy nuclei. The electron field operator satisfies the Dirac equation

$$\left[\vec{\alpha}\cdot(\vec{p}+\vec{A}) + \beta - A_o\right]\psi = i\,\frac{\partial\psi}{\partial t} \qquad (5)$$

while the electromagnetic four-potential satisfies

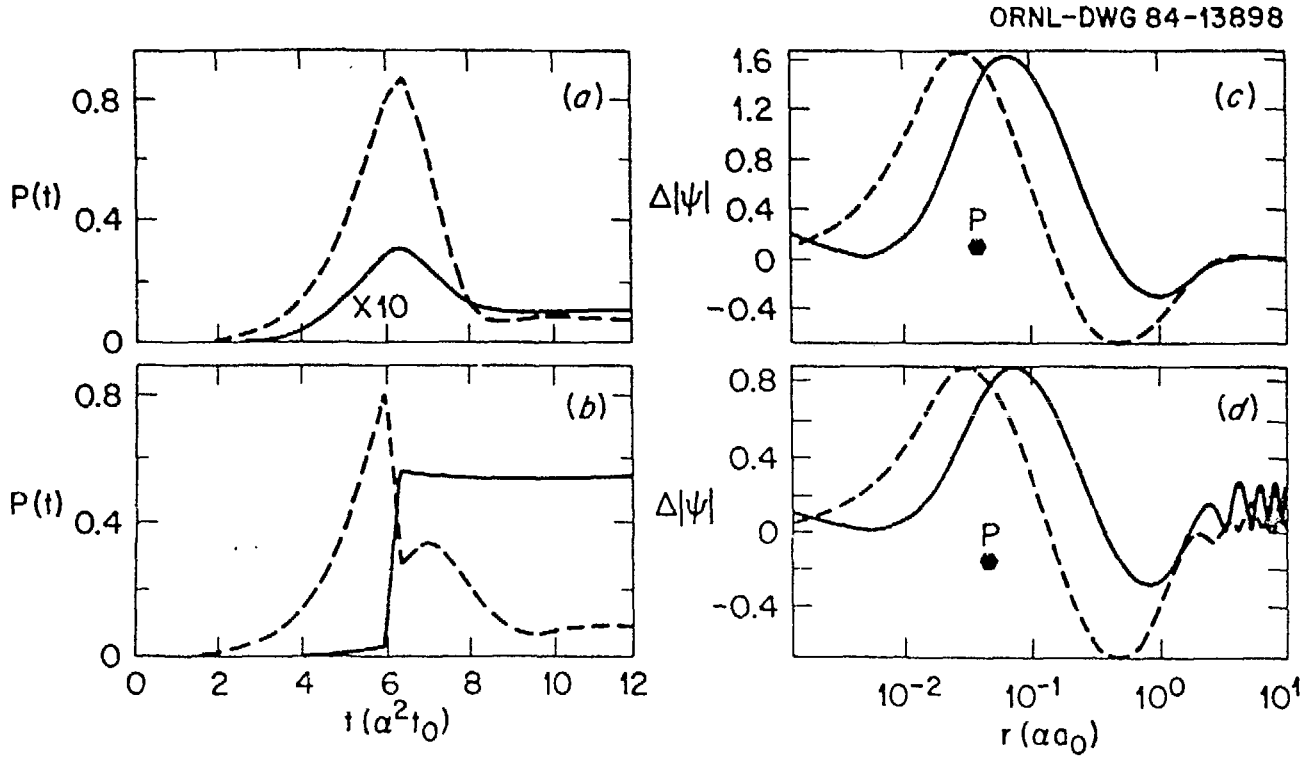

Fig. 3. U + Cm head-on collision at a bombarding energy of 6.05 MeV per particle. (a),(b): time evolution of the positron (full line) and electron (dotted line) probabilities in the finite element basis, respectively with and without, a time delay of T = 50 $\alpha^2 t_0$ occurring at t = 6 $\alpha^2 t_0$. (c),(d) shows the change from the initial state in the modulus of the 1s wavefunction vs. the distance from the target nucleus before and after a time delay of T = 50 $\alpha^2 t_0$; full and dotted lines refer to the large and small wavefunction components, G and F. P denotes the position of the projectile nucleus.

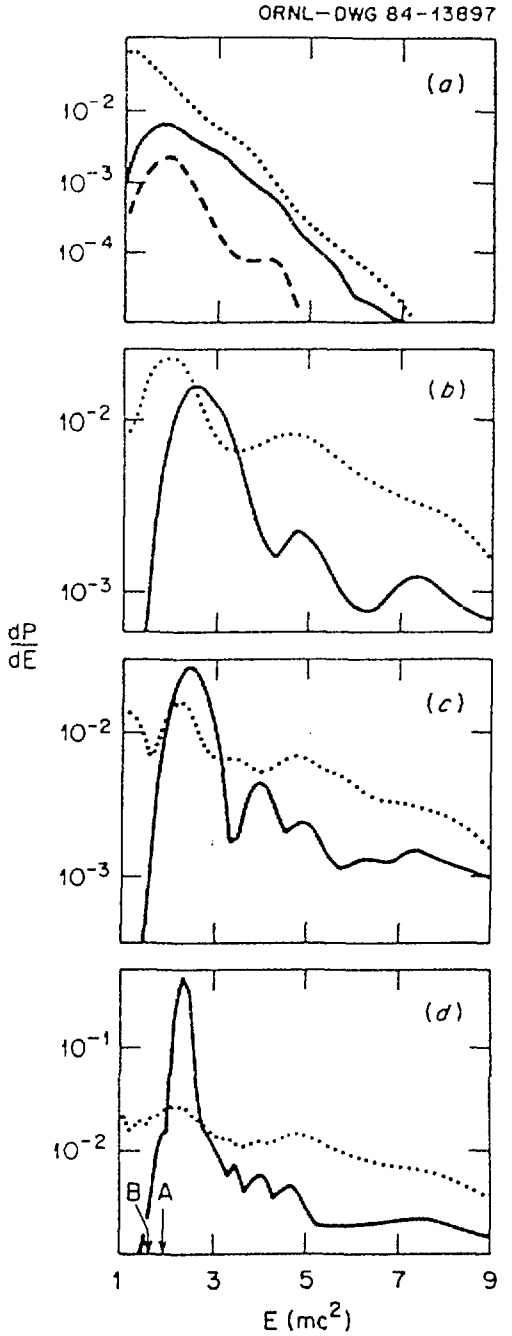

Fig. 4. U + Cm head-on collision at a bombarding energy of 6.05 MeV per particle. Positron (full line) and electron (dotted line) spectra in the target frame, in units of $1/mc^2$ per collision, for (a): no time delay; (b), (c), (d) respectively T = 2.5, 5, 20 $\alpha^2 t_o$. The positron spectrum for b=19 fm is shown by the dashed line in (a). In (d) the arrows A,B indicate the peak position in a head-on U+Pu collision, and a U+Cm collision at b = 19 fm (both at the same bombarding energy.

$$\Box A_\mu = \bar{J}^{ext} + \psi^\dagger \alpha_\mu \psi \quad (6)$$

where ψ and A are field operators. For the appropriate choice of gauge, (5) and (6) contain most of quantum electrodynamics. For electrons moving independently in strong external fields, we are justified in treating A as a classical field, using a wavefunction expansion for ψ, and the expectation of the current operator on the righthand side of (6).

The first step in solving (5) and (6) is to retain only the external source as the righthand side of (6). Then we have only to solve the one-particle Dirac equation with a prescribed retarded potential. In a subsequent section we shall present the results of such calculations for a one-dimensional (1D) model. The next step would be to restore the mean lepton current on the righthand side of (6) and propagate A self-consistently with ψ, thus obtaining a time-dependent Dirac Hartree (TDDH) theory. We shall outline the algorithms needed for such a program, though calculations are not yet complete.

Of necessity, (5) and (6) must be solved numerically. For the reasons given in Section 2, the numerical procedure will represent the wavefunctions and the potentials on a spatial mesh. We shall then demand that the algorithms satisfy two criteria which we shall term fidelity and plausibility. Fidelity means that the finite numerical representation of (5) and (6) goes uniformly to the continuous limit as the density of mesh points becomes infinite. A less formal statement is that the discrete equations must have an intuitive correspondence with their continuous counterparts. Plausibility means that the discrete equations imply well-behaved finite analogues of the correspondence principle for the Dirac fields

$$(p+A)^2 \psi = \psi \tag{7}$$

with current conservation and the gauge condition,

$$\partial^\mu J_\mu^{tot} = 0 \quad , \quad \partial^\mu A_\mu = 0. \tag{8}$$

Our view is that (7) and (8), as well as (5) and (6), form the set of discrete equations which must all be satisfied in order to obtain a plausible physical interpretation.

In order to test our numerical methods and obtain some feeling for the physics of relativistic heavy-ion collisions, we have introduced a 1D simplification of (5)-(8). The target T is at rest while the projectile P moves at a velocity v. The target and projectile potentials in their rest frames are cut off Coulomb fields

$$V_C = - \frac{Q_C}{\left(x^2 + a_C^{\,2}\right)^{1/2}} \quad (C = T,P). \tag{9}$$

The wavefunction reduces to a two-component spinor associated with the Hamiltonian

$$H_D = \begin{bmatrix} m - A_o & -\frac{\partial}{\partial x} - iA_x \\ \frac{\partial}{\partial x} + iA_x & -m - A_o \end{bmatrix} \tag{10}$$

where the potentials are given by

$$A_o = -V_T(x) - \gamma\, V_p[\gamma(x-vt)] \tag{11}$$

$$A_x = \gamma\, v\, V_p[\gamma(x-vt)] \tag{12}$$

To save writing indices, we shall write the components of the two potentials as $(A_o, A_x) = (\phi, a)$ and the components of the two-current $(J_o, J_x) = (\rho, j)$ where ρ is the normal electron density.

$$\rho = \psi^{\dagger}\psi. \tag{13}$$

From (10) we deduce the conservation of the current

$$\frac{\partial \rho}{\partial t} = -\frac{\partial j}{\partial x} \tag{14}$$

where

$$j = \psi^{\dagger}\begin{pmatrix} 0 & -1 \\ i & 0 \end{pmatrix}\psi = -i(j_{+} - j_{-}) \tag{15}$$

We have indicated that the current is naturally written as the sum of two complex entities. Then the vector potential satisfies,

$$\left(\frac{\partial^2}{\partial t^2} - \frac{\partial^2}{\partial x^2}\right)a = j^{ext} + j. \tag{16}$$

A similar equation relates ϕ and ρ, whence the gauge condition follows,

$$\frac{\partial \phi}{\partial t} = -\frac{\partial a}{\partial x}. \tag{17}$$

Our next task is to derive a faithful and plausible numerical representation of (10) and (16).

BASIS SPLINE COLLOCATION METHODS

We shall expand the unknown functions (e.g. ψ) in basis splines (often called B-splines) and determine the expansion coefficients by collocation. This combination of techniques represents the state of the art for solving partial differential equations in other fields.[4,5] At this time, we shall only outline the method: details will be given elsewhere.

As an exercise, consider the 1D non-relativistic Schroedinger equation,

$$[T + V(x)]\psi = H\psi = i\frac{\partial \psi}{\partial t} \tag{18}$$

We choose a set of points $\{x_j\}$ $\{1 \leq j \leq n\}$ known as "knots" and on the subset $(k \leq j \leq k+N-1)$ construct a piecewise continuous and $(N-1)$ differentiable polynomal, which is zero outside the interval. This function $u_k^{(N)}(x)$ is the N-th order basis spline: Fig. 5 shows a quadratic (N=3) function. The linear superposition

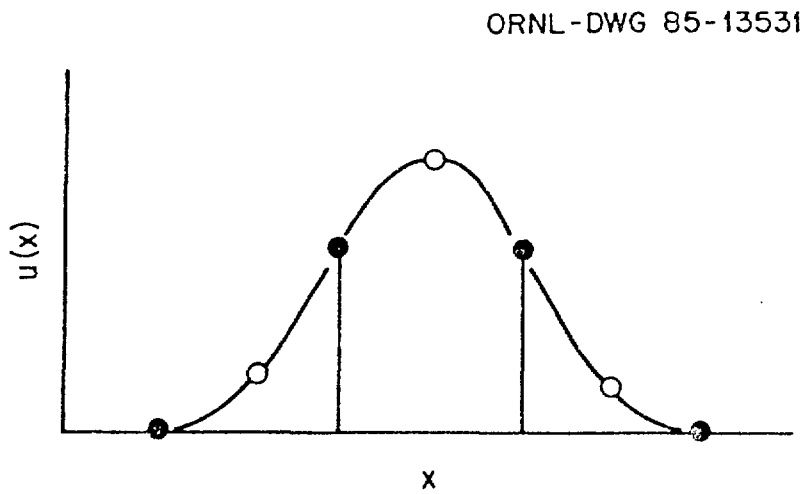

Fig. 5. Quadratic (third order) basis spline. The knots are indicated by the filled circles and the collocation points by the open circles.

$$\psi(x) = \sum_{k=1}^{n} \psi^k u_k(x) \tag{19}$$

provides a spline approximation to ψ on an interval spanned by the subset of the knots. In the collocation method we demand that (18) be satisfied at a set of points $\{\xi_\alpha\}$ $(i < \alpha < n)$ known as "data" or "collocation" points. The choice

$$\xi_\alpha = \frac{1}{2}\left(x_{\alpha+\mu} + x_{\alpha+\mu+1}\right), \quad \mu = [N/2] \tag{20}$$

is adequate for N odd. The number of collocation points must equal the number of functions in (19), so that the coefficients may be eliminated in favor of the values of ψ at the collocation points,

$$\psi_\alpha = \psi(\xi_\alpha) = \sum_k \psi^k B_{\alpha k}. \tag{21}$$

The matrix B acts like a metric,

$$B_{\alpha k} = u_k(\xi_\alpha) \quad , \quad B^{k\alpha} = \left[B^{-1}\right]_{k\alpha} \tag{22}$$

$$\psi^k = \sum \psi_\alpha B^{k\alpha}. \tag{23}$$

Inserting (19) in (18) and eliminating ψ^k, we find the collocation representation of the Schroedinger equation,

$$\sum_{\beta} H_{\alpha}{}^{\beta}\, \psi_{\beta} = i\, \frac{\partial \psi_{\alpha}}{\partial t} \tag{24}$$

$$H_{\alpha}{}^{\beta} = T_{\alpha}{}^{\beta} + V_{\alpha}{}^{\beta} \quad , \quad V_{\alpha}{}^{\beta} = \delta_{\alpha\beta}\, V(\xi_{\alpha}) \tag{25}$$

$$T_{\alpha}{}^{\beta} = -\frac{1}{2} \sum_{k} B''_{\alpha k}\, B^{k\beta} \quad , \quad B''_{\alpha k} = u_k''(\xi_{\alpha}). \tag{26}$$

We immediately note that local operators, e.g. V, are represented by diagonal matrices of their values at the collocation points: this apparently trivial result coexists with the more sophisticated functional representation (19). The complexities arise in the kinetic energy matrix, though the non-sparse form of (26) is actually an advantage, in that the metric B spreads the large elements of B over a wide band on either side of the diagonal. As a consequence, the largest eigenvalue of H is much smaller than in other expansion methods. We should also remark that no overlap matrix appears on the righthand side of (24). However, the matrix H is, in general, unsymmetric, requiring the introduction of both direct and adjoint solutions. Most theorems used for symmetric self-adjoint methods have analogs for collocation methods; however, they are somewhat more difficult to state and prove.

We shall jump ahead a little and write down the adjoint problem before considering the Dirac equation in detail. Using matrix notation (24) becomes

$$i\, \frac{\partial}{\partial t}\, \underline{\psi} = \underline{\underline{H}}\, \underline{\psi} \tag{27}$$

The adjoint eigenvector is defined as the solution of

$$i\, \frac{\partial}{\partial t}\, \underline{\phi} = \underline{\underline{H}}^{\dagger} \underline{\phi}. \tag{28}$$

It readily follows that the norm

$$Q = \underline{\phi}^{\dagger} \underline{\psi} = \sum \phi_{\alpha}^{*} \psi_{\alpha} \tag{29}$$

is conserved in time: conventionally Q = 1. The expectation of any operator is given by

$$\langle \Omega \rangle = \underline{\phi}^{\dagger} \underline{\underline{\Omega}} \underline{\psi} = \sum \phi_{\alpha}^{*} \Omega_{\alpha}{}^{\beta} \psi_{\beta} \tag{30}$$

where $\Omega_{\alpha}{}^{\beta}$ is constructed according to the prescription

$$\Omega_{\alpha}{}^{\beta} = \sum \Omega_{\alpha k} B^{k\beta} \quad , \quad \Omega_{\alpha k} = (\Omega u_k)_{\xi_{\alpha}} \tag{31}$$

of which (24) is a special case. In particular, if Ω is a local function of position,

$$\Omega_{\alpha}^{\ \beta} = \delta_{\alpha\beta}\Omega(\xi_{\alpha}) \tag{32}$$

A general feature of collocation methods is illustrated by (29), that regardless of the basis or knot sequence, the metric for constructing the norm is just a Kronecker delta function. It is a further corollary that the particle density associated with each collocation point is given by

$$\rho_{\alpha} = \phi_{\alpha}^{*}\psi_{\alpha} \tag{33}$$

To propagate (27) over a small time interval, we use an exponential propagator constructed by means of a power series,

$$\underset{\sim}{\psi}(t+\tau) = \exp\left[-i\tau\underset{\sim}{H}\left(t + \frac{1}{2}\tau\right)\right]\underset{\sim}{\psi}(t). \tag{34}$$

With a reasonable choice of τ, there is no difficulty in satisfying (29) to one part in 10^{12}.

Finally we point out that it is a simple matter to extend the foregoing formalism to more than one dimension. The expansion (19) now uses products, e.g. in 2D

$$\psi(x,y) = \sum \psi^{k_1k_2} u_{k_1}(x)u_{k_2}(y) \tag{35}$$

these are sometimes called "tensor" splines.[4] The Hamiltonian (25) and (26) is now generalized to

$$\begin{aligned} H_{\alpha_1\alpha_2}^{\beta_1\beta_2} &= \left(T_x\right)_{\alpha_1}^{\beta_1}\delta_{\alpha_2\beta_2} + \left(T_y\right)_{\alpha_2}^{\beta_2}\delta_{\alpha_1\beta_1} \\ &\quad + V(\xi_{\alpha_1},\xi_{\alpha_2})\delta_{\alpha_1\beta_1}\delta_{\alpha_2\beta_2} \end{aligned} \tag{36}$$

Again the potential energy is completely diagonal while the kinetic energy breaks into small blocks. The structure of (36) is exceedingly simple when compared to other methods of comparable accuracy.

APPLICATION TO THE DIRAC EQUATION

Unfortunately it is not possible to apply directly to (10) the prescription which led to (26). This would lead head on to the "Fermion Doubling" pathology,[6] which we will now briefly explain. Suppose we write the Dirac equation corresponding to (10) for a free particle in terms of the large and small components, $\psi = (G,F)$,

$$G' = (m+E)F \quad , \quad F' = (m-E)G. \tag{37}$$

If the derivatives are replaced by the simplest finite difference formulae on a mesh $x = jh$ $(1 < j < n)$

$$(G')_j = (G_{j+1} - G_{j-1})/2h \tag{38}$$

we have to solve the difference equation

$$G_{j+2} - 2G_j + G_{j-2} = 4h^2 (m^2 - E^2)G_j \tag{39}$$

A solution of (39) is given by

$$G_j = \exp(ik_\lambda x_j) \quad , \quad k_\lambda = \frac{\lambda\pi}{nh} \tag{40}$$

where we have imposed periodic boundary conditions. However, the eigenvalue

$$E_\lambda^2 = m^2 + \frac{1}{h^2} \sin^2 \left(\frac{\lambda\pi}{n}\right) \tag{41}$$

is also associated with another solution

$$\tilde{G}_j = (-1)^j G_j \tag{42}$$

of unphysical momentum $k_\lambda + (\pi/h)$.

The doubled spectrum (42) appears in all numerical formulations. For time integrations its existence has serious consequences: high momentum components appear more or less at random and grow exponentially. In a stationary problem the spurious solutions can be avoided by eliminating the small component and discretizing an equivalent Schroedinger equation. This is usually not practical for time evolution problems, and in any case, does not extirpate the problem at its root. Our analysis is that (39) is unacceptable as a mass-energy dispersion relation, since it has unphysical solutions. The discrete Dirac equation should be a factorization of a correct dispersion relation,

$$G_{j+1} - 2G_j + G_{j-1} = h^2(m^2 - E^2)G_j \tag{43}$$

This is one part of our requirement of plausibility introduced in Section 3.

Our first attempt to address this problem[2] consisted in using forward and backward differences to discretize the two parts of (37),

$$F_{j+1} - F_j = h(m-E)G_j \quad , \quad G_j - G_{j-1} = h(m+E)F_j. \tag{44}$$

Thus hermiticity is preserved and (43) follows. It might be thought that a generalization of (44) to an arbitrarily complicated discretization scheme, e.g. that described in Section 4, would be difficult to find. We have been fortunate to arrive at a prescription which is entirely satisfactory in practice. Given a representation of the

non-relativistic kinetic energy, e.g. (26), we make an LU decomposition (lower-upper triangular),

$$T = -\frac{1}{2} \underset{\sim}{D}_- \underset{\sim}{D}_+ \tag{45}$$

The decomposition is uniquely specified if

$$D^-_{\alpha\alpha} = \left| D^+_{\alpha\alpha} \right| \tag{46}$$

The matrices $D_\pm$ are those used to represent the first derivative in (10). A special case is provided by (44), since it is easily verified (using an obvious notation for tridiagonal matrices) that

$$(1,-2,1) = (-1,1,0)(0,-1,1). \tag{47}$$

Among the possible decompositions, (45) is favored because it always gives a faithful representation of the first derivatives (as in (47)), in the sense of Section 4. We shall return to this point below. It is useful to remark that the elements of $D_\pm$ in the first and last rows define boundary conditions, though we do not have space to go into more detail here.

The basis spline collocation representation of (10) is now constructed from (25) and (26). The potentials are diagonal matrices of their values at the collocation points. The kinetic energy (26) is factorized according to (45) to get the derivative matrices. Then

$$\underset{\sim}{H}_D = \begin{bmatrix} m-\underset{\sim}{A}_o & -\underset{\sim}{D}_+ - i\underset{\sim}{A}_x \\ \underset{\sim}{D}_- + i\underset{\sim}{A}_x & -m-\underset{\sim}{A}_o \end{bmatrix}. \tag{48}$$

Propagation in time is accomplished by applying (34) to (27) and (28).

We suggested in Section 3 that conservation of flux (14) is an important part of solving the complete problem. This requires an appropriate definition of the current, which in turn requires further discussion of the $D_\pm$ matrices. If these are faithful representations of the first derivative, each column sum must be approximately zero (except for the column containing only one non-zero element): we can show that if the diagonal elements are slightly modified to make the column sum exactly zero, these matrices acquire unusual properties. An algorithm, such as (34), which employs ascending powers of $D_\pm$ is hardly affected by the modification: inverse powers are a different matter. Consider the sequence of vectors defined by

$$\underset{\sim}{D}^T_+ \underset{\sim}{\omega}^+_{\mu+1} = \underset{\sim}{\omega}^+_\mu \quad , \quad \left(\omega^+_o\right)_\alpha = \delta_{\alpha 1} \tag{49}$$

with the new definition, it is identically true that

$$\left(\omega^+_1\right)_\alpha = 1 \tag{50}$$

while, to a good approximation,

$$\left(\omega^{+}_{\mu+1}\right)_{\alpha} \simeq \xi^{\mu}_{\alpha}/\mu! . \tag{51}$$

Analogous relations may be derived for D_. The content of (50) is that the inverse of differentiation is integration with the metric (29); (51) generalizes this statement to iterated integrals (Dirichlet's formula). For physics, the significant consequence of (49)-(51) is that the manipulations leading to conservation laws (Green's theorem, etc.) now have a rigorous analog on a finite mesh. The key lemma deduced from (49) is that

$$\left(\underset{\sim}{\omega}^{+}_{\mu+1}\right)^{T}\underset{\sim}{f} = \left(\underset{\sim}{\omega}^{+}_{\mu}\right)^{T}\underset{\sim}{g} \quad \text{if } \underset{\sim}{f} = \underset{\sim}{D}_{+}\underset{\sim}{g}. \tag{52}$$

Some examples will be given below.

To derive a current operator, we begin with the density (33), which is a vector in collocation space whose components may be written

$$\rho_{\lambda} = \underset{\sim}{\phi}^{\dagger}\underset{\sim}{\Pi}_{\lambda}\underset{\sim}{\psi} \quad , \quad \left(\Pi_{\lambda}\right)_{\alpha\beta} = \delta_{\lambda\alpha}\delta_{\lambda\beta} \tag{53}$$

Then from (27), (28), (48), and (53) we find that

$$\frac{\partial\rho_{\lambda}}{\partial t} = i\left(f^{+}_{\lambda} - f^{-}_{\lambda}\right) \tag{54}$$

where

$$f^{\pm}_{\lambda} = \underset{\sim}{\phi}^{\dagger}_{G}\left[\underset{\sim}{\Pi}_{\lambda}, \underset{\sim}{D}_{\pm}\right]\underset{\sim}{\psi}_{F} \tag{55}$$

(G, F again refer to large, small components; upper, lower subscripts to +, -.) If we define current vectors (in general complex) by

$$\underset{\sim}{j}_{\pm} = \underset{\sim}{D}^{-1}_{\pm}\ \underset{\sim}{f}_{\pm} \tag{56}$$

(14) and (15) are replaced by the discrete flux conservation theorem,

$$\dot{\underset{\sim}{\rho}} = i\left(\underset{\sim}{D}_{+}\underset{\sim}{j}_{+} - \underset{\sim}{D}_{-}\underset{\sim}{j}_{-}\right) \tag{57}$$

From (52) and (57) it follows that

$$\frac{\partial}{\partial t}\left(\underset{\sim}{\omega}^{T}_{1}\underset{\sim}{\rho}\right) = i\left(j^{+}_{1} - j^{-}_{n}\right). \tag{58}$$

We have examined the case of a bound system moving with a uniform velocity in the observer's frame, for which the form of the

current operator is the density times the velocity. The prescription (55)-(57) reproduces the correct result to better than 1% for a reasonable mesh spacing providing (50) is satisfied.

The final mark of plausibility is the gauge condition (17). Suppose (16) has the finite representation

$$\left(\frac{\partial^2}{\partial t^2} - \underset{\sim}{\Delta}^2\right)\underset{\sim}{a} = \underset{\sim}{j}(t). \tag{59}$$

In a 2D or 3D model problem Δ^2 is a sum of matrices: the notation does not imply that an explicit form of Δ is available. To propagate (59) in time, we invoke the solution of a driven harmonic oscillator, so that

$$\begin{aligned}\underset{\sim}{a}(\tau) = \underset{\sim}{\Delta}^{-2}\,[\cosh(\underset{\sim}{\Delta}\tau)-1]\underset{\sim}{j}(\tau/2) \\ + \cosh(\underset{\sim}{\Delta}\tau)\underset{\sim}{a}(0) + \underset{\sim}{\Delta}^{-1}\sinh(\underset{\sim}{\Delta}\tau)\dot{\underset{\sim}{a}}(0)\end{aligned} \tag{60}$$

with error $O(\tau^3)$ over a small interval τ. The operators in (60) are all power series in Δ^2, which may thus be applied in 2D or 3D.

Let us define

$$\underset{\sim}{a} = -i\left(\underset{\sim}{a}_+ - \underset{\sim}{a}_-\right) \tag{61}$$

where $a_\pm$ are generated by the sources $j_\pm$ using representations $\Delta_\pm^2$ of the Laplacian; ϕ is generated from ρ. Then by analogy with (57),

$$\underset{\sim}{\phi} = i\left(\underset{\sim}{D}_+\underset{\sim}{a}_+ - \underset{\sim}{D}_-a_-\right) \tag{62}$$

if and only if

$$\left[\underset{\sim}{D}_\pm, \underset{\sim}{\Delta}_\pm^2\right] = 0. \tag{63}$$

The simplest way of satisfying (63) is just to make Δ identical with D, i.e. to make $a_\pm$ satisfy

$$\left(\frac{\partial^2}{\partial t^2} - \underset{\sim}{D}_\pm^2\right)\underset{\sim}{a}_\pm = \underset{\sim}{j}. \tag{64}$$

Applying (52), we obtain a discrete form of Gauss's theorem: in the static limit

$$\omega_1^T j_+ = -\left(D_+ a_+\right)_1 \quad , \quad \omega_1^T j_- = -\left(D_- a_-\right)_n. \tag{65}$$

In 2D or 3D, $\Delta_\pm^2$ would have a block form similar to (36), but still lower or upper triangular. This LU property makes the static analog of (64) vastly more attractive than Possion's equation discretized in a conventional manner.

ANALYSIS OF FINAL STATE PROBABILITIES

We have made calculations on the 1D model explained in Section 3. Our procedure is to solve (3) numerically and then project on a set of final eigenstates to obtain the probabilities (4). The geometry of a collision is illustrated in Fig. 6. The target is fixed at T, while the projectile starts at P_0 and ends at P. The mesh extends from x=-L to x=L. In the final configuration we project on eigenstates of the target and moving projectile separately. Though everyone has a clear intuitive picture of bound and continuum states associated with either the target or projectile, the mathematical and computational description of these states has always been problematic. We translate our intuition directly by introducing a spatial projection of the final-state wavefunction into parts associated with the target and projectile,

$$\psi_T = \Omega(-x)\psi \quad , \quad \psi_P = \Omega(x)\psi \tag{66}$$

where

$$\begin{aligned} \Omega(x) &= 0 && x < 0 \\ &= 1 && x > L\theta \\ &= \frac{1}{2}\left[1-\cos\left(\frac{\pi x}{L\theta}\right)\right] && 0 < x < L\theta \end{aligned} \tag{67}$$

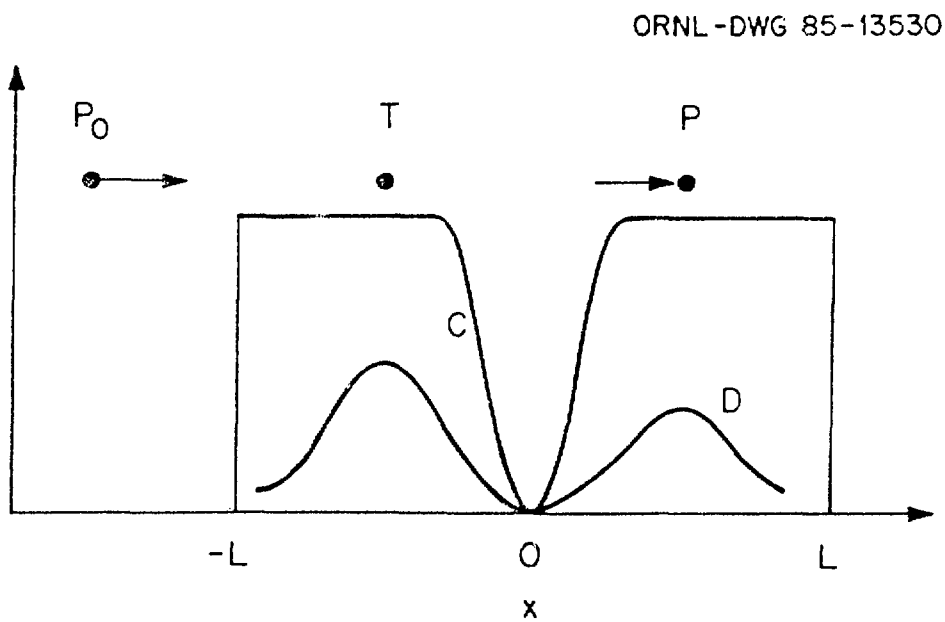

Fig. 6. Geometry of a 1D collision. We show the position of the target (T) and the initial and final positions of the projectile (P_0,P) relative to the box $-L < x < L$. D is a schematic final state which has been folded into the cosine bell C.

The "cosine bell" shape of Ω minimizes spurious Fourier components due to discontinuties at $x = 0$; we normally take $\theta = 0.2$.

The target probabilities are calculated by projecting ψ_T on the discrete eigenstates of the target alone (spanning both bound and continuum states) calculated on the part of the mesh spanning $-L < x < 0$. Projectile probabilities are calculated by projecting on the discrete eigenstates of the moving projectile alone, calculated on the part of the mesh spanning $0 < x < L$.

The discretization techniques explained in Sections 4 and 5 reduce the stationary Dirac equation in the observer's (fixed) frame to a matrix eigenvalue problem. To obtain the projectile eigenstates in a frame moving with the projectile, requires that we introduce the Lorentz transformation of the Dirac spinor.[7] Let (x',t') denote the frame moving with a velocity v and (x,t) the observer's frame: the Lorentz transformation is given by

$$x' = \gamma(x-vt) \quad , \quad t' = \gamma(t-vx) \tag{68}$$

where

$$\gamma = (1-v^2)^{-1/2} = \cosh\omega. \tag{69}$$

A spinor $\psi(x,t)$ in the moving frame appears to the observer as

$$\psi' = S(-v)\psi(x't') \tag{70}$$

where

$$S(v) = \exp\ (1/2\ \omega\alpha) = \cosh\ \omega/2 + \alpha\ \sinh\ \omega/2 \tag{71}$$

and in the representation (10)

$$\alpha = \begin{pmatrix} 0 & -i \\ i & 0 \end{pmatrix} \tag{72}$$

Thus consider a stationary state in the moving frame which satisfies

$$H_D'\ \phi_o = \varepsilon_o \phi_o \tag{73}$$

This appears as

$$\psi' = \exp[-i\varepsilon_o\gamma(t-vx)]S(-v)\phi_o[\gamma(x-vt)]. \tag{74}$$

In the non-relativistic limit, $\gamma \to 1$ and $\varepsilon_o \to 1$, to $O(v^2)$, so we recover the familiar result

$$\psi'_{NR} = \exp(ivx)\phi_o(x-vt)\exp(-it). \tag{75}$$

To obtain a consistent finite representation of (74), we introduce the "boosted" Dirac equation

$$[H_D(x',p) - vp]\psi' = [\varepsilon_o/\gamma]\psi'. \tag{76}$$

The projectile eigenstates are obtained by setting up the usual discrete representation of (76) in the fixed frame and solving the resulting matrix eigenvalue problem.

Before leaving this section, we should clear up some technicalities associated with the projection (4). If the wavefunction is propagated in the direct representation (27), we must solve the eigenvalue problem in the adjoint representation,

$$\underset{\sim}{H}_D^{fT} \underset{\sim}{\phi}_n^f = \varepsilon_n \underset{\sim}{\phi}_n^f \tag{77}$$

where f specifies that the final state of either the projectile or target is being considered; we will omit the superscript henceforth in the interests of clarity. The final state probabilities are given by

$$p_n = \left|\phi_n^\dagger \psi\right|^2 \tag{78}$$

if the norm (29) is unity.

If ε_n corresponds to a bound state, the interpretation of (78) is clear. For ε_n in the "box" continuum, we construct a differential probability by interpolating

$$\frac{dp}{d\varepsilon}\left[\varepsilon = \frac{1}{2}\left(\varepsilon_{n+1} + \varepsilon_n\right)\right] = \frac{\frac{1}{2}\left(p_{n+1} + p_n\right)}{\left(\varepsilon_{n+1} - \varepsilon_n\right)}. \tag{79}$$

We further want to distinguish between electrons moving to the right or left. This can be done by observing that the box continuum states tend to be alternately of approximately even or odd character with respect to reflection about the center of the box. By combining these pairs, we can make up eigenfunctions which satisfy

$$\hat{R}\ \psi^{\pm} = \left(\psi^{\pm}\right)^* \tag{80}$$

to a good approximation, $\hat{R}$ being the space reflection operator. Thus, if $n = 2m$, we diagonalize R in the basis $\left(\phi_n, \phi_{n+1}\right)$ to obtain

$$\hat{R}\ \phi_m^c \simeq \phi_m^c \quad , \quad \hat{R}\ \phi_m^s \simeq -\phi_m^s \tag{81}$$

whence

$$\psi_m^{\pm} = \frac{1}{\sqrt{2}}\left(\phi_m^c \pm i\phi_m^s\right) \tag{82}$$

are approximately eigenstates of positive and negative momentum, respectively.

NUMERICAL RESULTS FROM THE ONE-DIMENSIONAL MODEL

We now describe calculations on the model defined by (9)-(12) with the specific choice of parameters:

$$Q_T = 1.0,\ Q_P = 0.9;\ a_T = a_P = 0.75. \tag{83}$$

The Dirac equation was discretized using the methods explained in Sections 4 and 5, particularly (45)-(48). Propagation in time was accomplished using (34). The interval $-15 < x < 15$ was covered by 150 equally spaced knots. Most of the calculations employed quadratic splines; some checks with quartic splines did not show any serious change in the numbers. The time step τ was chosen so that $0.01 > v\tau > 0.003$.

Accuracy was investigated by studying an isolated moving atom and by considering various meshes. The norm (29) was always conserved to better than one in 10^{10}, from which we conclude that propagation in time is not a source of error for practical purposes. Sensitivity of probabilities to the mesh spacing was 1-5%. However, sensitivity to the size of the box was 10-30%. The larger estimates apply to smaller probabilities. We conclude that efforts to improve accuracy should focus on the location of the finite boundary. It is worth remarking that, by comparison to the earlier studies using finite elements, the solutions exhibited very little noise outside the physical interaction region. It appears that this sensitivity to boundary conditions is an artifact of the primitive discretization algorithms.

The results will be more readily understood if we consider the momentum distribution in the initial (ground) state of the target. Figure 7 shows this distribution for the positive and negative energy components of the 1s state of Cm; our model ground state has very similar features. For the positive components, the mean momentum $\overline{p} = 0.76$ corrsponding to $\beta = 0.6$ (130 KeV, 240 MeV/u beam energy); for negative components $\overline{p} = 1.27$ whence $\beta = 0.8$ (320 KeV, 580 MeV/u beam energy). Thus, symmetric charge capture by a bare nucleus of similar charge will take place where the relative velocities of the electron components match, i.e. about $\beta = 0.6$. Figure 7 shows why the spontaneous emission of positrons is dominant for $\beta < 0.4$: here no matching momentum components are available. However, the dynamical emission, particularly in the projectile frame is increasingly probable above $\beta = 0.4$ and persists to very high energies. The energy spectrum of the spontaneous positron emission (Fig. 4) is essentially the negative energy distribution from united nuclei, so that the resemblence to Fig. 7 is not coincidental. If the "box" is defined by $-L < x < L$, where $L \sim 15$ (the units are those explained in Section 2), we conventionally take the target nucleus to be fixed at $-L/2$, while the projectile moves from $x = -3L/2$ to $+L/2$ in the course of a collision (Fig. 6). Figures 8, 9, and 10 show the squared components $|G|^2$ and $|F|^2$ of the spinor ψ as functions of x for the projectile velocities $v = 0.4, 0.8, 0.98$ ($\psi = 1.09, 1.67, 5.03$; bombarding energy = 0.08, 0.63, 3.8 GeV/u). The evolution of the wavefunction as the collision proceeds is indicated in three frames, which

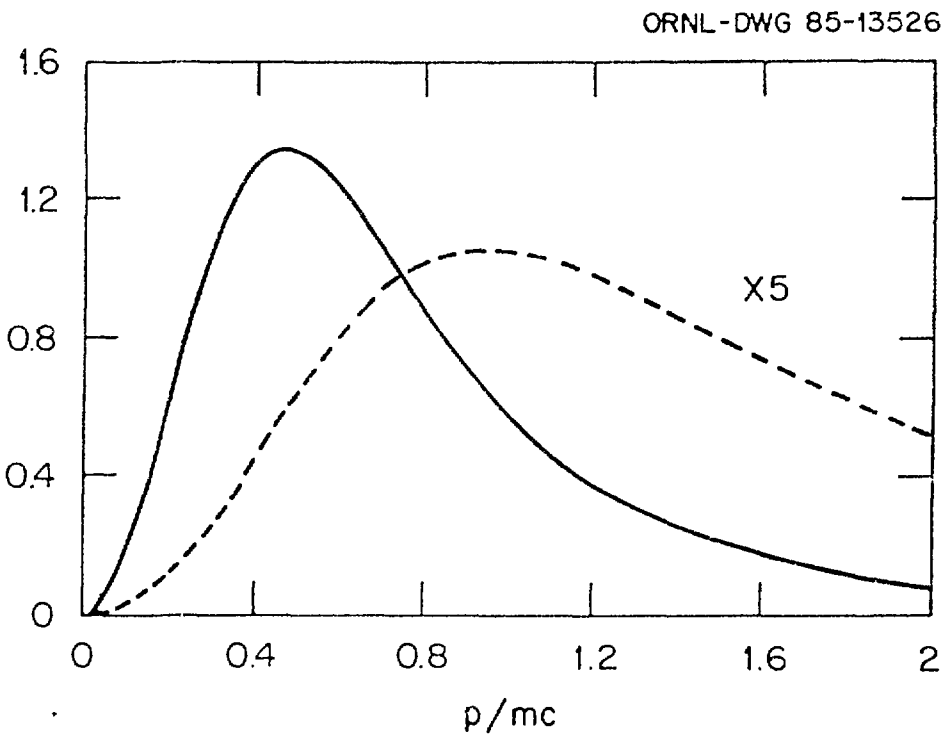

Fig. 7. Momentum distributions for the positive (full line) and negative (dotted line) energy components of the 1s orbital of Cm.

also show the corresponding position of the projectile. Figure 11a-11c shows the time evolution of probabilities for the collisions illustrated in the preceeding figures: specifically we have plotted the quantities (78) summed over the target positive and negative energy continua. At the lowest velocity, the system is responding nearly adiabatically, as suggested by the oscillations as the probabilities relax to their final values. At the highest velocity, the system behaves impulsively, the probabilities relaxing to small final values without oscillating: in the range v = 0.5-0.9 the projectile velocity matches the main components in the initial state wavefunction (Fig. 7) so that the inelastic probabilities do not relax but resonate in the final state at large values. Though G and F are mixed in electron and positron eigenstates, perusal of Figs. 8-10 does suggest qualitative phenomena. Thus, in Fig. 9 we notice that G is large between the nuclei, suggesting a high probability of finding electrons near the projectile. By contrast, the prominence of F ahead of the projectile in Fig. 10 suggests positron formation in this frame of reference.

The processes considered are the formation of bound, positive energy continuum and negative energy continuum states, described in (1), (2), and Fig. 1. In summary,

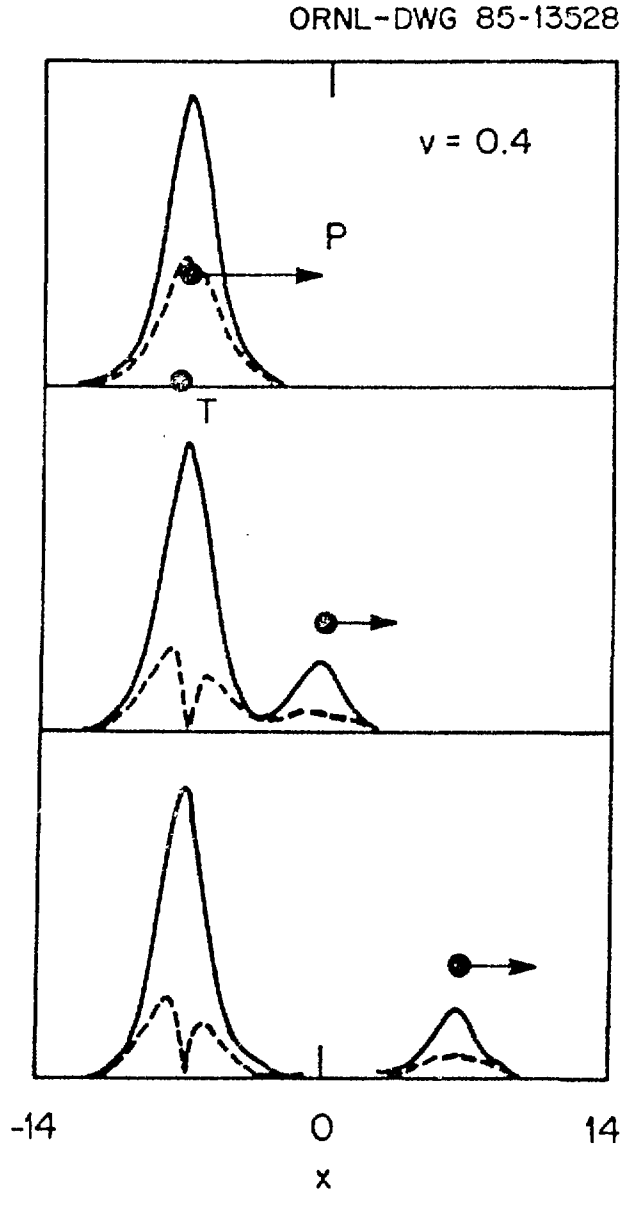

Fig. 8. Time evolution of the particle density in space for a collision at v = 0.4. $|G|^2$ and $|F|^2$ are shown by full and dotted lines. P and T denote the projectile and target nuclei: the passage of time in the three frames is indicated by the placement of P.

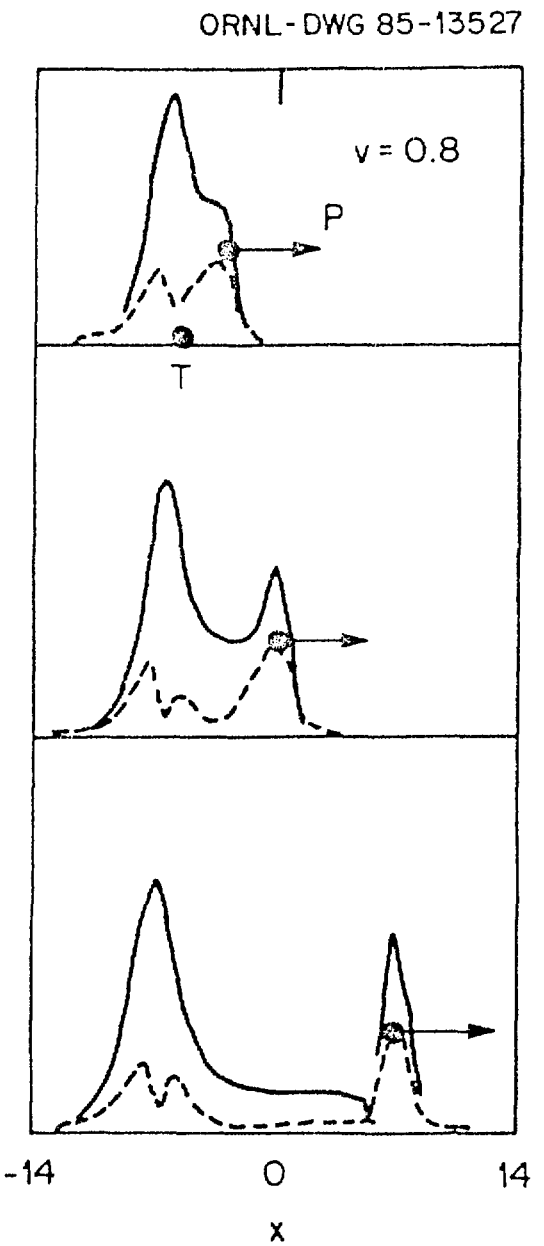

Fig. 9. Same as Fig. 8 with v = 0.8.

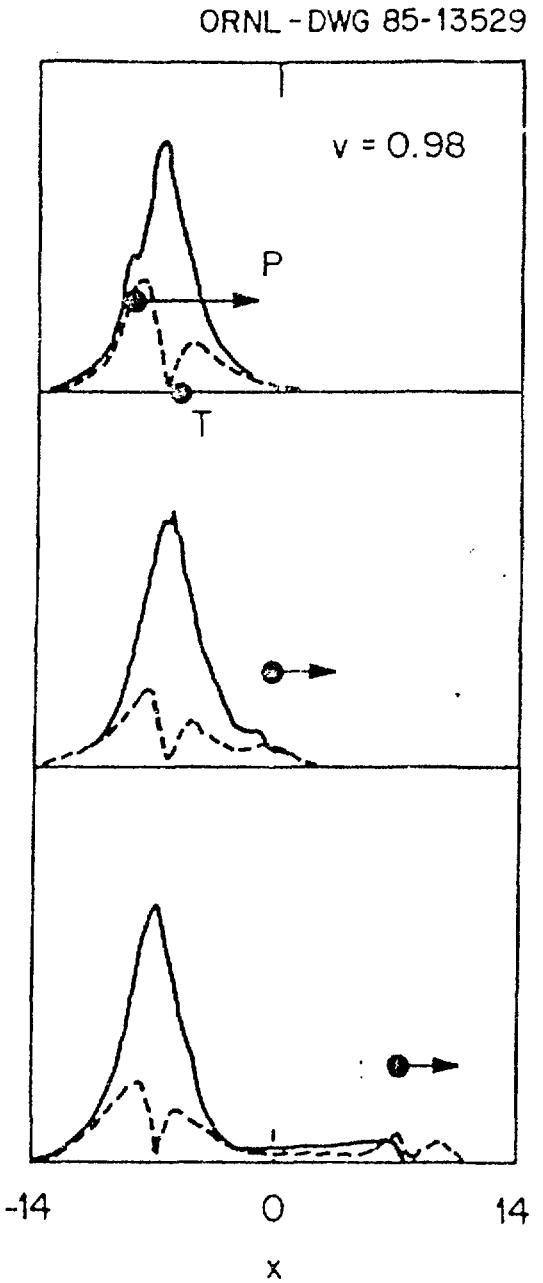

Fig. 10. Same as Fig. 8 with v = 0.98.

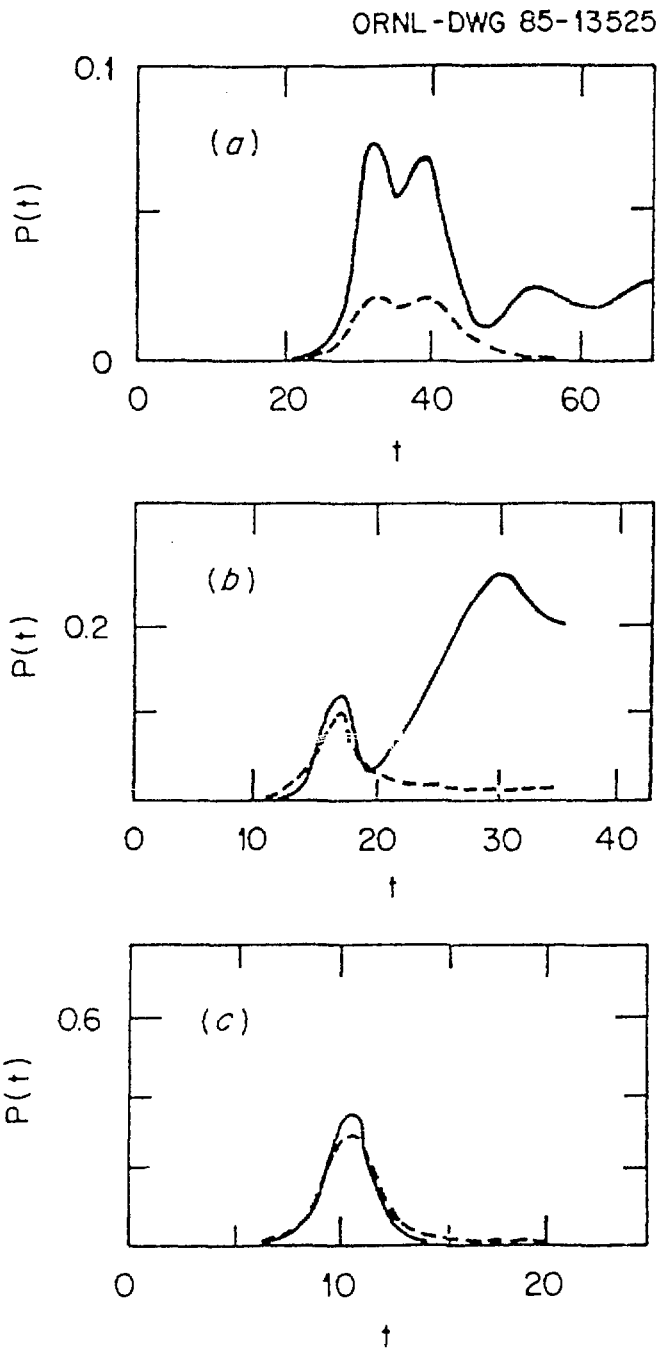

Fig. 11. Probabilities associated with positive (full lines) and negative (dotted lines) energy continua of the target are plotted as a function of time for the collisions considered in Figs. 8-10: (a) $v = 0.4$, (b) $v = 0.8$, and (c) $v = 0.98$.

$$
\begin{aligned}
P + T(1) &\rightarrow P + T(n > 1) \\
&\quad P + [T + e^{\pm}] \\
&\quad P(n > 1) + T \\
&\quad [P + e^{\pm}] + T
\end{aligned}
\tag{84}
$$

Figures 12 and 13 show a variety of probabilities in the projectile and target frames, as functions of projectile velocity. The most striking results are the extent of capture into the ground state of the projectile and the extent of positron production in both frames of reference. Figure 14 shows the combined positron and delta-electron production in both frames, and the total inelastic probability which is dominated by capture.

Finally, in Figs. 15 and 16 we show the energy spectra of electron and positrons in the target and projectile frames for v = 0.8. Right- and left-moving particles are distinguished using the algorithms (78)-(82). Considerable left-right asymmetry is observed in all cases. The oscillations seen in the left and right components separately are due to rescattering by the nuclei: the flux removed from one component reappears in the other component, so the total shows little effect. An attenuated form of the same phenomena[8] is responsible for the cusp asymmetry in real 3D systems. The striking

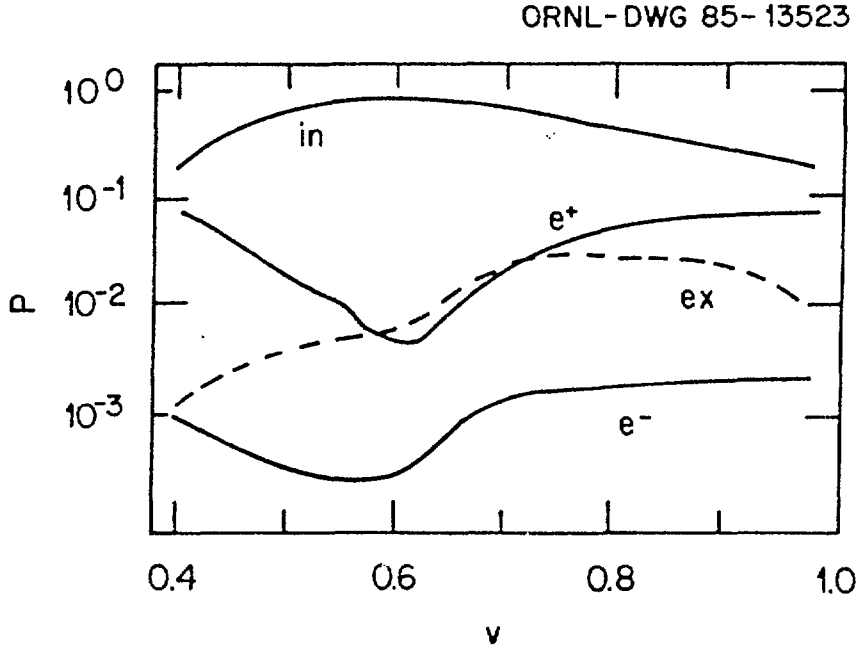

Fig. 12. Final-state probabilities in the target frame as functions of the projectile velocity: (in) total inelastic; (ex) excited bound states of the target; (e^-) positive energy continuum (electrons); (e^+) negative energy continuum (positrons).

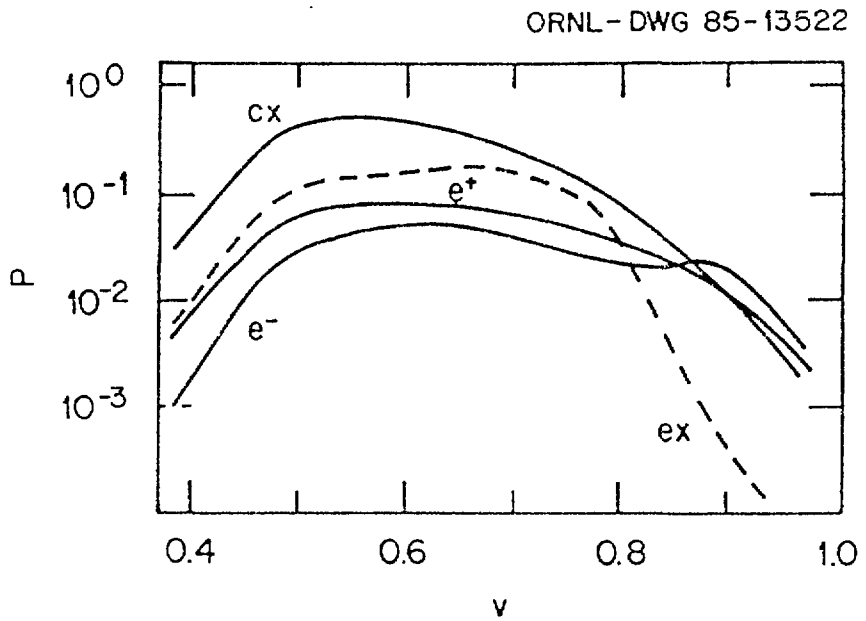

Fig. 13. Final-state probabilities in the projectile frame as functions of the projectile velocity: (cx) capture into the projectile ground state; (ex) excited bound states of the projectile: (e^-) positive energy continuum (electrons); (e^+) negative energy continuum (positrons).

feature here is the enhancement of the rightward and the suppression of the leftward positrons in the projectile frame, Fig. 16b. While electrons are captured, it appears that positrons are repelled into the continuum. Furthermore, they are repelled into the forward direction. More realistic calculations are needed, but it is plausible to speculate that such directional emission of positrons may be observed experimentally forward of the projectile.

We conclude by listing some processes of interest in heavy ion colliders together with estimates of their probabilities in the range 0.1 to 3.0 GeV/u, based on our model. P denotes a bare projectile, T(lab) denotes a fixed target experiment and K(KK) one (two) filled K orbits.

(a) P + T(lab) → T X-ray + anything:

dominated by capture, probability approaches unity.

(b) P + T(lab) → δ-electron + anything:

probability small, usually < 0.05.

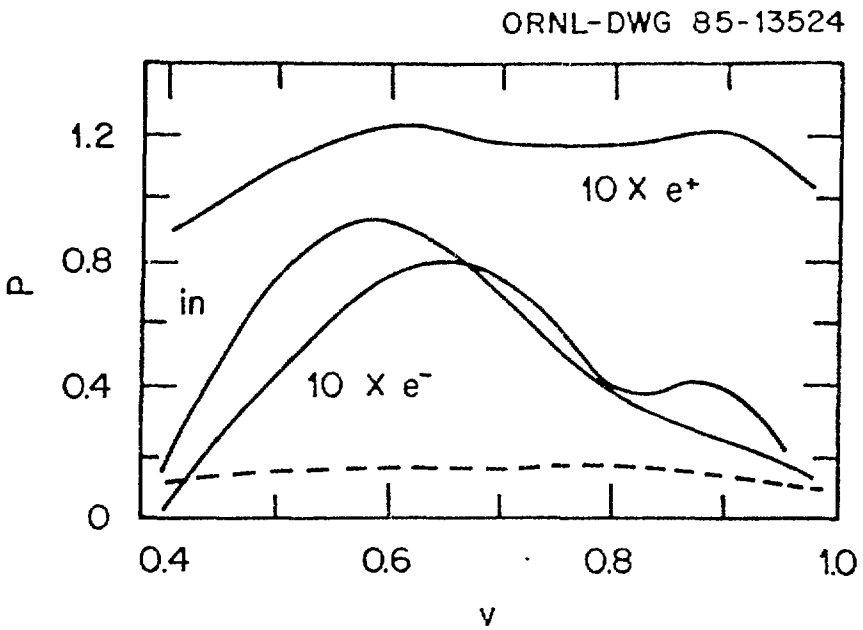

Fig. 14. Combined final-state probabilities for the target and projectile frames as functions of the projectile velocity: (in) total inelastic; (e^-) positive energy continuum (electrons); (e^+) negative energy continuum (positrons). The flux lost by folding with the cosine bell is shown by the dashed line.

(c) $P + T(lab) \rightarrow P_K + e^+ + anything,\ P_{KK} + e^+ + anything.$

This process can take place with or without capture from T; in either case, probability < 0.05.

(d) $P + T \rightarrow P_K + T + e^+,\ P + T_K + e^+$

probability < 0.1 either way.

Clearly more realistic calculations are needed. However, we can convert the above head-on probabilities to cross sections by conservatively estimating that relativistic processes take place within nuclear separations[1,2] of about 100 fm, corresponding to a perfectly absorbing cross section of 100 barns. The resulting estimates are not far out of line with those discussed by H. Gould elsewhere in this volume for higher energies. We note that at these energies (~100 GeV) pair production will occur predominantly by direct excitation out of the negative continuum.

We can also say something about heavy ion inertial confinement. Optimal beam energies are those for which the energy deposition is as large as possible, while the target is not yet transparent. From Figs. 12-14 this is probably about 1 GeV/u.

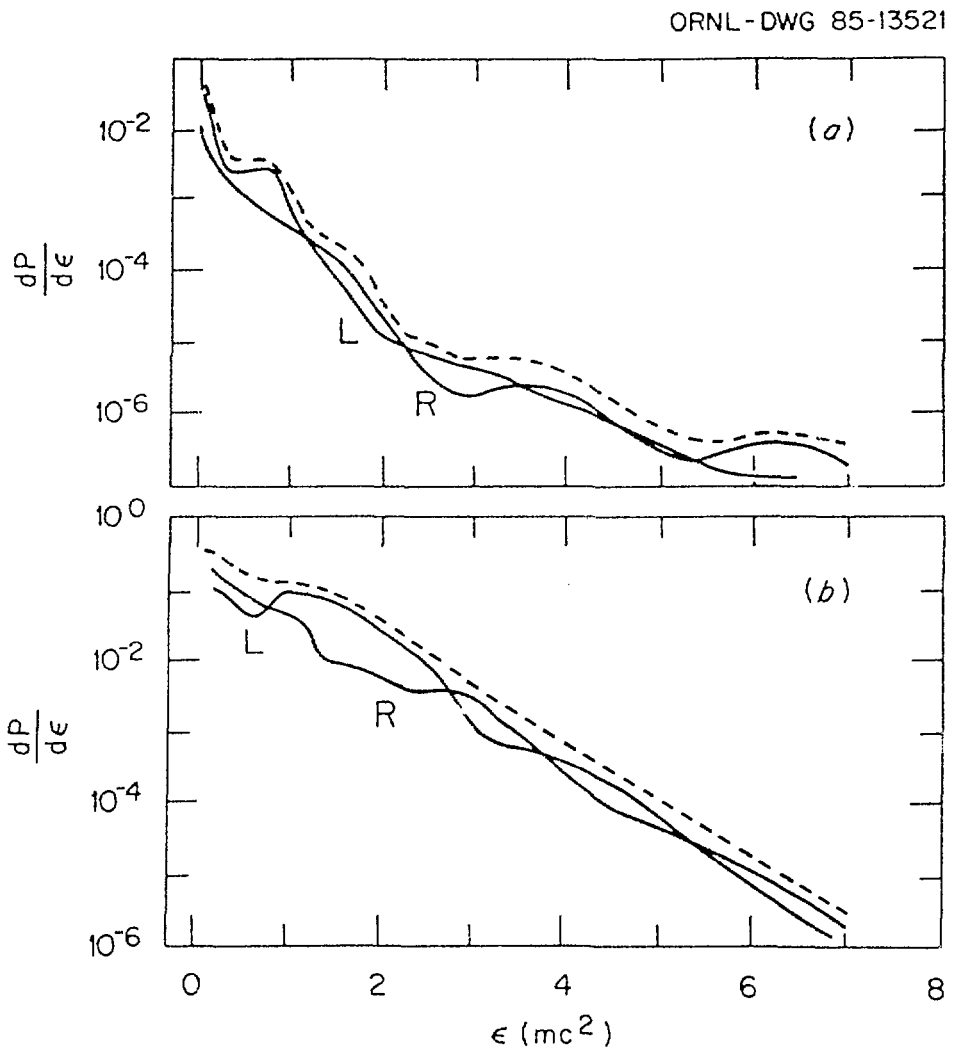

Fig. 15. Energy spectra as functions of kinetic energy in the target frame for v = 0.8: (A) electrons; (B) positrons. The right and leftwards momentum components are labelled R,L and their sum is shown as a dashed line.

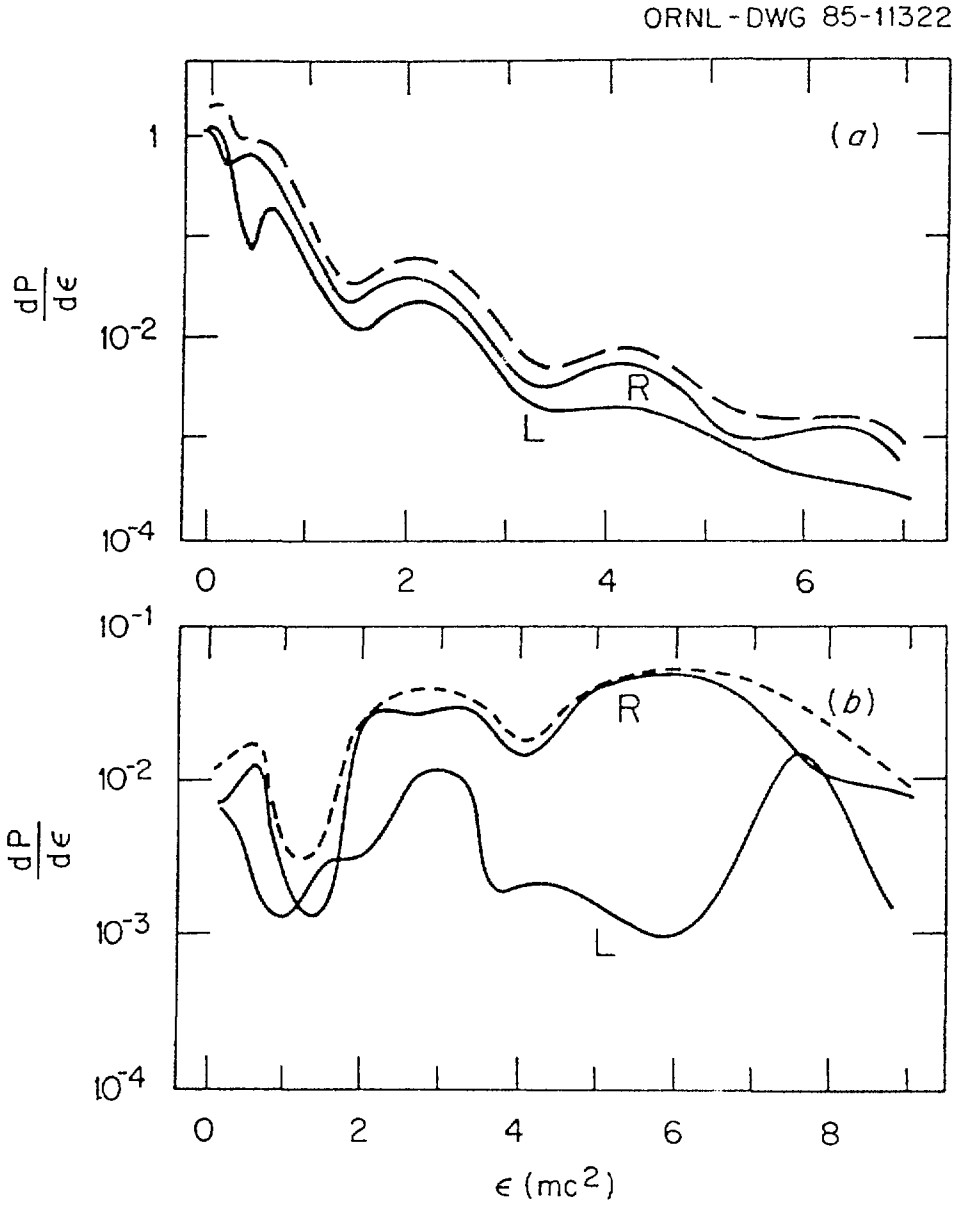

Fig. 16. Same as in Fig. 15 except for the projectile frame.

REFERENCES

1. "Quantum Electrodynamics of Strong Fields", ed. W. Greiner, Plenum Press, New York, 1983.

2. C. Bottcher and M. R. Strayer, Phys. Rev. Letts. 54, 669 (1985).

3. P.A.M. Dirac, "The Principles of Quantum Mechanics" (4th edn.), Claraendon Press, Oxford, 1958.

4. Carl de Boor, "A Practical Guide To Splines", Springer-Verlag, New York, 1978.

5. C.A.J. Fletcher, "Computational Galerkin Methods", Springer-Verlag, New York, 1984.

6. C. M. Bender and D. H. Sharp, Phys. Rev. Letts. 50, 1535 (1983).

7. Claude Itzykson and Jean-Bernard Zuber, "Quantum Field Theory", McGraw-Hill, New York, 1980.

8. R. Shakeshaft and L. Spruch, Phys. Rev. A20, 376 (1979); C. Bottcher, Phys. Rev. Lett. 48, 85 (1982).